A&A, 704, A322 (2025)
https://doi.org/10.1051/0004-6361/202453235

Astronomy & Astrophysics

HR-pyPopStar

II. High-spectral-resolution evolutionary synthesis models, low-metallicity expansion, and the properties of the stellar populations of dwarf galaxies

I. Millán-Irigoyen[1,⋆], M. Mollá[2], M. Cerviño[3], and M. L. García-Vargas[4]

[1] Max-Planck Institut für Astrophysik, 85741 Garching, Germany
[2] Departamento de Investigación Básica, CIEMAT, Av. Complutense 40, E-28040 Madrid, Spain
[3] Centro de Astrobiología (CSIC/INTA), ESAC Campus, Camino Bajo del Castillo s/n, E-28692 Villanueva de la Cañada, Spain
[4] FRACTAL S.L.N.E., C/ Tulipán 2, p13, 1A, E-28231 Las Rozas de Madrid, Spain

Received 29 November 2024 / Accepted 27 September 2025

ABSTRACT

Context. Low-metallicity stellar populations are very abundant in the Universe, either as the remnants of the past history of the Milky Way or similar spiral galaxies, or the young low-metallicity stellar populations that are being observed in the local dwarf galaxies or in the high-z objects with low metal content recently found with JWST.

Aims. Our goal is to develop new high-spectral-resolution models tailored for low-metallicity environments and apply them to the analysis of stellar population data, particularly in cases in which a significant portion of the stellar content exhibits low metallicity.

Methods. We used the state-of-the-art stellar population synthesis code HR-pyPopStar with available stellar libraries to create a new set of models focused on low-metallicity stellar populations.

Results. We compared the new spectral energy distributions with the previous models of HR-pyPopStar for solar metallicity. Once we verified that the spectra, except for the oldest ones that show some differences in the molecular bands of the TiO and G band, are similar, we re-analysed the high-resolution data from the globular cluster M 15 by finding a better estimate of its age and metallicity. Finally, we analysed a sub-sample of mostly star-forming dwarf galaxies from the MaNGA survey, we found a similar stellar mass-mean stellar metallicity weighted by light to other studies that studied star-forming dwarf galaxies and a slightly higher mean stellar metallicity than the other works that analysed all types of dwarf galaxies at the same time, but that are within the error bars.

Key words. stars: atmospheres – stars: evolution – galaxies: evolution – galaxies: star clusters: general – galaxies: stellar content

1. Introduction

The spectrophotometric properties of galaxies have been used for decades to study their formation and evolution processes. The analysis of the spectra and its interpretation are usually done using evolutionary synthesis models that create the spectral energy distribution (SED) and the associated data of the so-called simple stellar populations (SSPs). A SSP is a group of stars that formed simultaneously from the same cloud with a fixed initial mass function (IMF), and thus all the stars of a SSP have the same age and initial chemical composition. The SED of a SSP is computed as the sum of all spectra of its individual constituent stars. The synthesis models also contain supplementary information, such as the magnitudes in different spectral bands and their corresponding colours or stellar spectral absorption line indices obtained from those synthetic spectra.

In this way, the observed spectra of a galaxy or a galactic region can be decomposed as the spectra of their building blocks, i.e. the SSPs. This technique allows us to obtain information about the studied galaxy or a galactic region; for example, the star formation history (SFH), metallicity enrichment history, formed stellar mass, current stellar mass, mean stellar metallicity, and mean stellar age. This method of analysis for the stellar spectrum of a galaxy or a galactic region is an inverse technique: the decomposition of the spectrum is obtained through a sum of SSPs by searching for the best combination of these that minimises the residuals. This is used in codes such as STARLIGHT (Cid Fernandes et al. 2005), VESPA (Tojeiro et al. 2007), PIPE3D (Sánchez et al. 2016a,b), PPXF (Cappellari & Emsellem 2004; Cappellari 2017), FIREFLY (Wilkinson et al. 2017), or FADO (Gomes & Papaderos 2018).

However, SSP spectra can also be added directly following the results of a chemical evolution model (CEM) applied to the study region, as in Mancone & Gonzalez (2012), Mollá (2014), Millán-Irigoyen et al. (2020). The direct method uses the star formation and metallicity enrichment histories predicted by the CEM, which are equivalent to the mass contributions of SSPs of each age and metallicity, necessary to calculate the final theoretical SED of the galaxy or a galactic region.

Irrespective of the analysis method, the spectra of the SSPs used in the analysis need to satisfy some requirements such as a spectral resolution similar to the observed spectrum of the object we want to analyse and a good completeness in the ages and metallicities of the possible stellar populations of the object. One of the most important requirements is the spectral resolution of the synthetic spectra of the SSPs, which must be at least similar to the spectral resolution of the observed spectra in order to avoid a loss of information in the process of the analysis.

If the synthetic spectra have a lower resolution than the data, it would be necessary to degrade the observed spectra (see Millán-Irigoyen et al. 2021, for a detailed explanation of

---

⋆ Corresponding author: imillan@mpa-garching.mpg.de

Table 1. Summary of some intermediate- and high-resolution SSP models in the literature, compared to the present work.

Reference	Code	Range (Å)	$\delta\lambda$ (Å)	$R_{\rm th}$	Z
LEB04	PEGASE-HR	4000–6800	0.55	9091	0.0002–0.05
GON05	Sed@	3000–7000	0.30	16 667	0.002–0.05
PER09	BASTI iso.	2500–10 500	1.00	5000	0.0001–0.04
M&S11	Maraston	1000–25 000	0.25	20 000	0.0001–0.04
VAZ16	MILES	1680–500 000	0.90	5556	0.0001–0.04
CON18	FSPS	3700–24 000	1.67	3000	0.00044–0.028
CBC20	GALAXEV	3540–7410	0.90	3000	0.0002–0.030
Ma20	Fuel-consumption code	3600–10 300	0.8–2.4	1800	0.00007–0.03
XSL		3500–24 000	0.12–0.8	10 000	0.0001–0.03
MI21	PYPOPSTAR	91–24 000	0.10	50 000	0.004–0.05
This work	PYPOPSTAR	2500–10 500	0.10	50 000	0.0001–0.05

Notes. References. LEB04: Le Borgne et al. (2004); GON05: González Delgado et al. (2005); PER09: Percival et al. (2009); M&S11: Maraston & Strömbäck (2011); VAZ16: Vazdekis et al. (2016); CON18: Conroy et al. (2018); CBC20: Coelho et al. (2020); Ma20: Maraston et al. (2020); MI21: Millán-Irigoyen et al. (2021); XSL: Verro et al. (2022).

the different definitions of spectral resolution). Thus, given the resolutions of state-of-the-art and future instruments that are partially or completely devoted to extragalactic studies in very large telescopes, such as MEGARA (GTC), WEAVE (WHT), VLT/MOONS (VLT), or MOSAIC (ELT), it is necessary to have a base of SSPs with a similar spectral resolving power (R) to the one of the instruments (R in the range of 18 000–20 000).

Another important requirement for the synthesis models is a wide coverage in both ages and metallicities to consider all the possible environments. The majority of galaxies in the Universe have SFHs with stellar populations with very different ages and metallicities coexisting.

A large number of works have been devoted to the synthesis of SSPs. Some of them are low-resolution models (Cerviño & Mas-Hesse 1994; Fioc & Rocca-Volmerange 1997; Kodama & Arimoto 1997; Leitherer et al. 1999; Bruzual & Charlot 2003; Maraston 2005; Fritze-v. Alvensleben & Bicker 2006; Eldridge & Stanway 2009; Conroy et al. 2009; Maraston et al. 2009; Fioc & Rocca-Volmerange 2019), and some of them use empirical libraries (Conroy & van Dokkum 2012; Vazdekis et al. 2015, 2016; Maraston et al. 2020). Well-known medium- to high-resolution synthesis models include those of Le Borgne et al. (2004), González Delgado et al. (2005), Coelho et al. (2007), Percival et al. (2009), Maraston & Strömbäck (2011), Conroy & van Dokkum (2012), Leitherer et al. (2014), Vazdekis et al. (2016), Conroy et al. (2018), and Coelho et al. (2020).

In Table 1, we summarise the current evolutionary synthesis models from the literature with a medium or high spectral resolution (considering only those with $R_{\rm th} \geq 1800$). The columns indicate: (1) the reference of each model, (2) the synthesis code used to compute the SED, (3) the wavelength range, (4) the wavelength step, $\delta\lambda$, at λ = 5000 Å, (5) the value $R_{\rm th} = \lambda/\delta\lambda$, as defined for theoretical models, at that wavelength, and (6) the metallicity range of each model.

POPSTAR models (Mollá et al. 2009; Martín-Manjón et al. 2010; García-Vargas et al. 2013, hereinafter MOL09, MAN10, GV13, respectively), based on previous works by Garcia (1994), García-Vargas et al. (1995, 1998), were especially computed to study young stellar clusters in regions of star formation, such as the STB99 models (Leitherer et al. 1999). However, PopStar models also included old stellar populations (age >2.0 Gyr) in their model set. Starting from this base, we have recently developed in Millán-Irigoyen et al. (2021, hereinafter MI21) an updated Python version of POPSTAR models called HR-PYPOPSTAR by producing high-resolution SSP models ($R_{\rm th,5000}$ = 50 000) for 106 ages in the range of $\log\tau$ = [5.0, 10.18] and four metallicities: Z = 0.004, 0.008, 0.02, and 0.05.

Low-metallicity stellar populations constitute a significant part of the stellar content of local dwarf galaxies given their relatively inefficient SFH. Given the amount of dwarf galaxies found in huge-volume surveys such as Mapping Nearby Galaxies at APO (MaNGA, Bundy et al. 2015) or Dark Energy Spectroscopic Instrument (DESI) (DESI Collaboration 2025), low-metallicity models that include young stellar populations are essential to properly study the stellar content of these galaxies. Thus, the development of low-metallicity high-wavelength-resolution models, which also encompasses the maximum possible range of ages, is important to correctly study this kind of system.

The main aim of the present work is to update our HR-PYPOPSTAR models by now including the library of stellar models from Munari et al. (2005), the new Potsdam Wolf-Rayet (PoWR) O and B stellar library, and the PHOENIX stellar library for cool stars. This allows us to make SSP models with lower metallicities than the set of models of the MI21 version, by including two more sets for Z = 0.0001 and Z = 0.0004, while maintaining the same spectral resolution as in those previous models.

The paper is structured as follows. We describe the model in Section 2, mainly introducing the stellar libraries used in this work and explaining the differences from our previous work. The resulting SEDs, the derived magnitudes and D4000s, the comparison with our previous models, and the comparison with other authors are described in Section 3. In Section 4, we analyse the spectra of the low-metallicity globular cluster M 15, and a survey of dwarf galaxies from the MaNGA sample, and we compare them with the results of different authors. Our conclusions are recapitulated in Section 5.

2. Model description

The main ingredients of any population synthesis code are the isochrones, which trace the stellar parameters of each star present in the SSP at a given age, the spectral library, or the collection of spectra for each type of star, and the IMF. We used here the same set of isochrones from the Padova group as in MI21,

Table 2. Summary of the stellar libraries used in this work for each isochrone of our models.

Isochrone	WR	O & B	Mun05	PHOENIX	Rauch03
0.0001	subSMC	subSMC	0.0001	0.0001	0.002
0.0004	subSMC	subSMC	0.0004	0.0004	0.002
0.004	SMC	SMC	0.004	0.004	0.002
0.008	LMC	LMC	0.008	0.008	0.02
0.02	solar	solar	0.02	0.02	0.02
0.05	solar	solar	0.05	0.05	0.02

Table 3. Summary of the differences in $T_{\rm eff}$ coverage and number of stars in the new and old models of O and B stars from PoWR group.

Z	$N_\star$ Old PoWR	$N_\star$ New PoWR
solar	200	174
LMC	191	200
SMC	192	240

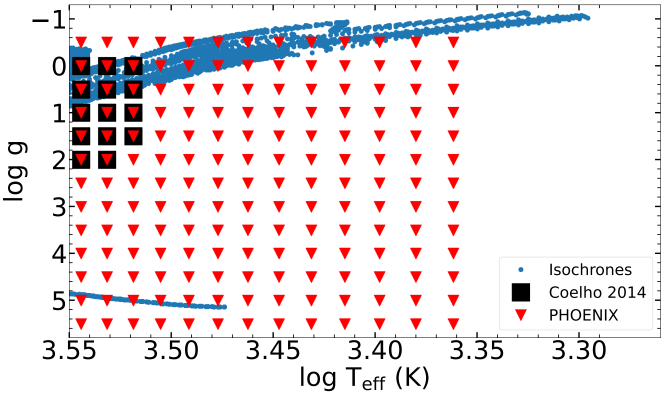

Fig. 1. Comparison of the coverage of the stellar libraries of C14, black squares, and PHOENIX, red triangles, for the low-temperature stars, $T_{\rm eff} < 4000$ K. The blue points represent the isochrones for all ages and solar metallicity.

(Bressan et al. 1993; Fagotto et al. 1994a,b; Girardi et al. 1996). However, instead of only using four metallicities, as in MI21, $Z = 0.004$, 0.008, 0.02, and 0.05, we added the isochrones of the two lowest metallicities, $Z = 0.0001$, and 0.0004.

2.1. Stellar libraries

Regarding the stellar libraries, we have the following stellar atmosphere classification: 1) Hot stars (O and B) with $T_{\rm eff} >$ 25 000 K; 2) Wolf-Rayet (WR) stars, defined using the surface abundance in the stellar atmosphere of C, N, O, and H; 3) 'cool' stars from A to G spectral types with $T_{\rm eff} \leq$ 25 000 K; 4) post-asymptotic giant branch (AGB) or planetary nebulae (PNe) stars; and 5) cool K and M stars.

The stellar libraries used in the population synthesis models and the metallicity range that each one has are summarised in Table 2. We explain each library and the change with respect to MI21. In the case of WR and post-AGB and PNe stars, we used the same libraries as in MI21, which cover the metallicity range from 0.002 to 0.05.

2.1.1. O and B type stars

For the O- and B-type stars, we used the new O- and B-stellar atmosphere models from PoWR. They computed the stellar atmospheres using the mass-loss recipe by Vink et al. (2001) divided by three, a mass-loss recipe that is more in agreement with current estimates of the stellar mass loss. They created models for four metallicities: solar, Large Magellanic Cloud (LMC), Small Magellanic Cloud (SMC), and sub-SMC ($1/31 Z_\odot$). We checked the spectra of all the models individually and removed the few that have non-physical emission line profiles that seem to be errors in the computation of the models and could affect the emission lines of the synthesised spectra. The comparison of the number of stars in each metallicity range for old and new versions of the models is described in Table 3.

2.1.2. A- to G-type stars

For A to G type stars, we substituted the stellar library from Coelho (2014, hereinafter C14) used in MI21 with the stellar models from Munari et al. (2005, hereinafter MUN05). These authors gave a set of synthetic spectra based on the code of Kurucz (2013) that covers the wavelength range from 2500 to 10 500 Å. These models are available for different combinations of stellar parameters, in particular the effective temperature, $T_{\rm eff}$, in the range $3500 \leq T_{\rm eff} \leq 47\,500$ K, with steps of 250 K up to 10 000 K, with progressively larger steps in $T_{\rm eff}$ for hotter stars, gravity in the range of $0.0 \leq \log g \leq 5.0$, metallicity in the interval $-2.5 \leq$ [M/H] ≤ 0.5, α-enhancement abundance from [α/Fe] = 0.0 and +0.4, three values of micro-turbulence velocity $\xi = 1$, 2, and 4 km s^{-1}, and stellar rotation in the range of $0 \leq V_{\rm rot} \leq 500$ km s^{-1}. We selected models with [α/Fe] = 0.0, $\xi = 2$ km s^{-1} and $V_{\rm rot} = 0$ km s^{-1}. Given that Kurucz models are not adequate to model hot stars where the approximations considered in them do not hold, we included only the stars of this library MUN05 with $T_{\rm eff} \leq 25\,000$ K. These models were originally computed at several spectral resolving powers, $R = 20\,000$, 11 500 (to simulate *Gaia* (Gaia Collaboration 2018)), 8500 (to simulate RAVE), and 2000 (to simulate SDSS/SLOAN), and a uniform dispersion of 1 and 10 Å pix^{-1}. For this particular work, we used the models with $R = 20\,000$.

2.1.3. K- and M-type stars

We included models for cool stars, spectral types K and M, using the PHOENIX atmosphere models (Husser et al. 2013) not used in MI21. These models simulate the 1D stellar atmosphere instead of using plane-parallel geometry. Moreover, they have an up-to-date list of atomic and molecular lines and a new equation of state. This allows them to more accurately model cool giant stars, especially in the red and near-infrared (NIR) parts of the spectra, where molecular bands are prominent. The PHOENIX library has a wider coverage of $T_{\rm eff}$ and $\log g$ on the HR diagram than the C14 library at low temperature. The comparison of coverage between C14 at low temperature and PHOENIX libraries with respect to the isochrones used in this work is shown in Fig. 1.

Since PHOENIX model atmospheres are computed with 1D spherical geometry, they have one more degree of freedom than plane-parallel models and require the stellar mass to determine the effective radius. Thus, for each model of the PHOENIX library that has $T_{\rm eff} < 4000$ K, we obtained the stellar radius from the header of the FITS file. Then, we computed the bolometric luminosity by integrating the spectra across its full wavelength range, 500−55 000 Å, and this computed stellar radius. We compared the luminosity we obtained with the bolometric luminosity also provided by the FITS header of each stellar atmosphere model.

We found that for giant stars ($\log g < 2.0$), the luminosities obtained this way are significantly lower than the bolometric luminosities of each model, in some cases accounting for just half of the bolometric luminosity. These discrepancies exceed the expected differences between the bolometric luminosity and the flux integrated over ultraviolet (UV), optical, and NIR bands, and they affect the fluxes of cool giant stars. As we use plane-parallel models for stars with $T_{\rm eff} < 25\,000$ K and want to preserve the luminosity of each star, we normalised the flux of giant stars, to make their integrated luminosity in the whole range of 500–55 000 Å match the bolometric luminosity of its model.

2.2. Initial mass function

We used the same four IMFs as in MI21: Salpeter (1955), Ferrini et al. (1990), Kroupa (2002, with a slope $\alpha = -2.7$ for massive stars), and Chabrier (2003), hereinafter referred to as SAL, FER, KRO, and CHA, respectively. In the following, we show the results using the CHA IMF, which is similar to the KRO IMF with $\alpha = 2.3$.

2.3. Stellar population synthesis

The spectrum of a SSP along an isochrone of a given age, τ_i, and metallicity, Z, was computed with the following equation:

$$F_{\lambda,{\rm SSP}}(Z,\tau_i) = \sum_{j=1}^{N_{\rm tot\,lib}(Z)} w_j(Z,\tau_i) \times F^{\rm lib}_{\lambda,j}(Z), \tag{1}$$

where $N_{\rm tot\,lib}(Z)$ is the number of elements in the stellar library with a given metallicity, Z, $F^{\rm lib}_{\lambda,j}(Z)$ is the monochromatic flux of the element, j, of the library with metallicity Z, and $w_j(Z,\tau_i)$ is the weight of each library element, j, for each point, i, of the isochrone of the corresponding metallicity, Z, and age.

The weight of each point, j, of the isochrone has a contribution given by the IMF and another one related to the correction of the luminosities of each point. The contribution of the IMF follows the equation

$$w_{\rm IMF}(m_j,Z,\tau_i) = \int_{m_{{\rm low},j}(Z,\tau_i)}^{m_{{\rm up},j}(Z,\tau_i)} \phi(m)dm, \tag{2}$$

where $m_{{\rm low},j}(Z,\tau_i)$ and $m_{{\rm up},j}(Z,\tau_i)$ define the mass intervals along the isochrone that share the same element, j, in the stellar library.

Furthermore, we had to correct the weights for each point of the isochrone, j, using the ratio between the bolometric luminosity of the isochrone, $L_{{\rm iso},j}$, and the integrated luminosity of the stellar library model, i. Thus, the total weight, $w_j(Z,\tau_i)$, is

$$w_j(Z,\tau_i) = w_{\rm IMF}(m_j,Z,\tau_i)\,\frac{L_{\rm iso}(m_i,Z,\tau_i)}{L^{\rm lib}_j(Z)}, \tag{3}$$

where $L^{\rm lib}_j(Z)$ is the integral over wavelength of $F^{\rm lib}_{\lambda,j}(Z)$ in the stellar library, which can be pre-computed or obtained from the parameters of the library. For plane-parallel non-expanding atmosphere models such as those from MUN05 or Rauch (2003), $F^{\rm lib}_{\lambda,j}(Z)$ is equivalent to the flux at the surface per surface unit cm^2, so we can calculate directly the luminosity for a given $T_{\rm eff}$ as

$$L_{\rm bol}/R^2 = \sigma_{\rm SB} T^4_{\rm eff}, \tag{4}$$

$\sigma_{\rm SB}$ being the Stefan-Boltzmann constant. This method is adequate for the MUN05 stellar library, whose spectral range from 2500 to 10 500 Å is too short to obtain the bolometric luminosity by integrating their spectra.

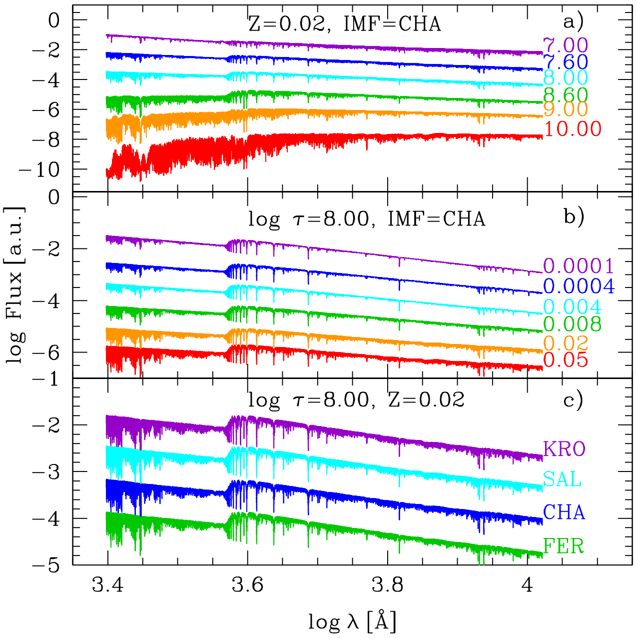

Fig. 2. SEDs obtained with this new version of the code HR-PYPOPSTAR. We show a comparison among SEDs with a) different ages (τ) for the same metallicity, $Z = 0.02$, and CHA IMF; b) different metallicities for a given age, $\log \tau = 8.00$, and CHA IMF; and c) different IMFs for a given age, $\log \tau = 8.00$, and metallicity, $Z = 0.02$.

We used the same assignment of an element, j, to each element, i, of the isochrone that was used in MI21. For groups 1), 3), and 4) we found the closest stellar model in $T_{\rm eff}$ and $\log g$; for WR stars we used the mass loss and the radius at a given optical depth (see details in MI21). The theoretical stellar libraries used in this work (see 2.1) have dense enough binning in the HR diagram to not produce problems in the synthesis. Regarding the old stellar population where cold stars dominate, the PHOENIX library coverage for the range 2300–4000 K in the $T_{\rm eff}$-$\log(g)$ diagram is given by steps of 100 K for $T_{\rm eff}$, and of 0.5 for $\log g$.

3. Results

3.1. Spectral energy distributions: Comparison with previous models

We produced the complete set of updated HR-PYPOPSTAR models using the four IMFs (SAL, FER, KRO and CHA), with 106 ages[1], and the six metallicities, Z = 0.0001, 0.0004, 0.004, 0.008, 0.02, and 0.05. The wavelength range is [2500 Å–10 500 Å] and the wavelength step is $\delta\lambda = 0.1$ Å. The resulting SEDs are publicly available on the web page of HR-PYPOPSTAR[2].

---

[1] The SAL IMF produces a shorter number of ages because lowest mass considered is 1 $M_\odot$.

[2] See in `https://www.fractal-es.com/PopStar`

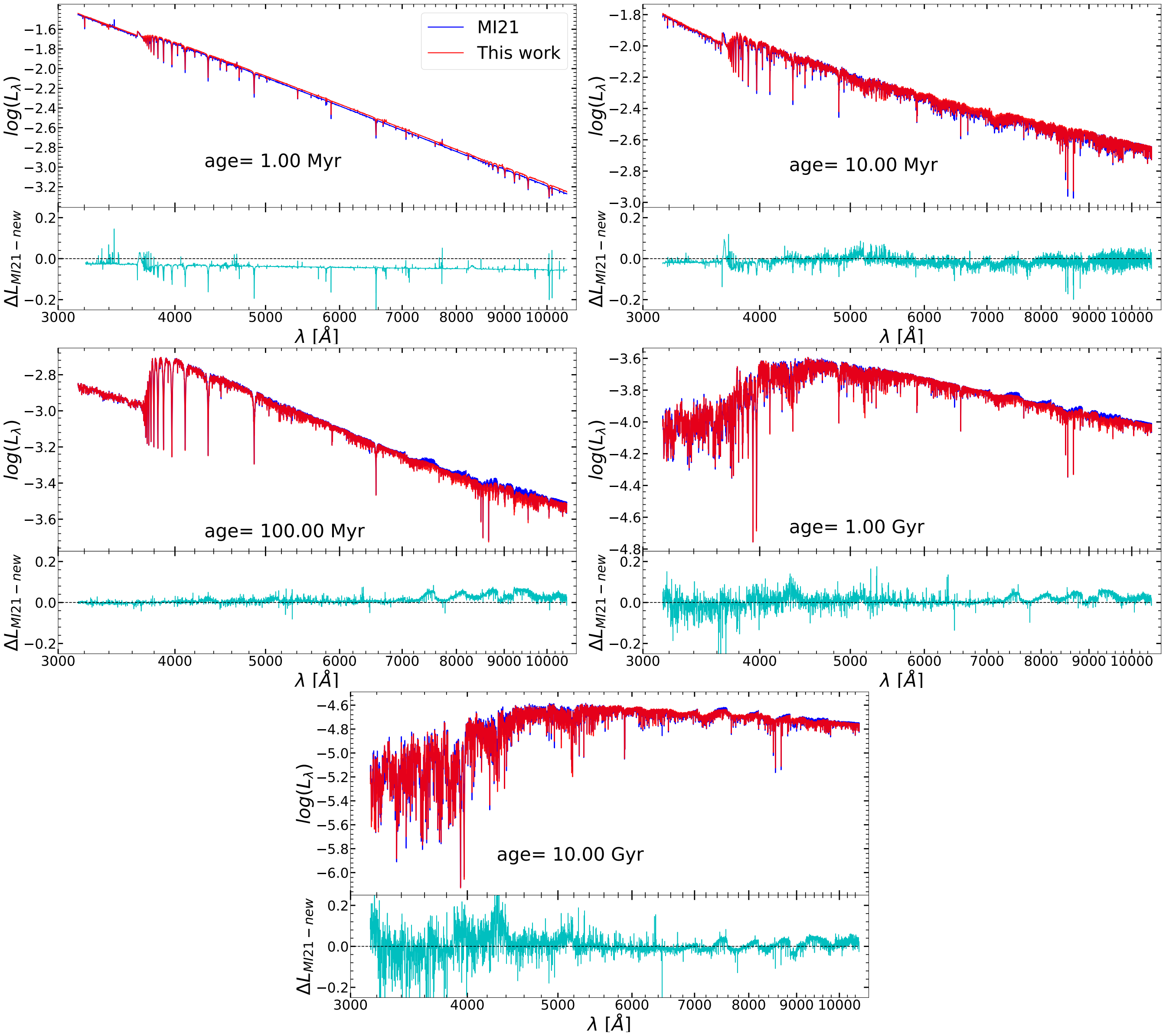

Fig. 3. Comparison between the old version of HR-pyPopStar using the stellar library of C14 (MI21), in a blue line, and the present models using MUN05 +PHOENIX stellar library, in a red line, for $Z = 0.02$ and CHA IMF. The bottom part of every sub-figure shows the residuals, $\Delta L_{\rm MI21-new} = \frac{L_{\rm MI21}-L_{\rm new}}{L_{\rm MI21}}$.

Figure 2 shows the SEDs with this version of HR-pyPopStar for: a) six selected ages at $Z = 0.02$, and the IMF from CHA; b) six different values of the metallicity, for a given age, $\tau = 100$ Myr, and the IMF from CHA; and c) four different IMFs with the same age, $\tau = 100$ Myr, and metallicity $Z = 0.02$. Each SED has an arbitrary shift on a logarithmic scale for the sake of clarity.

Then, we compared the effect of using different stellar libraries in the synthesis models. In order to do that, we compared the new SEDs created for this paper with the ones from MI21 for metallicity $Z = 0.02$ and the IMF of CHA for some specific ages: 1, 10, 100, 1000, and 10 000 Myr in Fig. 3.

For the age of 1 Myr, the new models have between 2 and 3% more luminosity than the MI21 ones. Moreover, there are notable changes in specific lines, such as the Balmer series and some other lines that even changed from emission to absorption and vice versa. These differences are attributed to the new models of O and B stars from PoWR group.

In the case of 10 Myr, the new models have a flux 3% higher than MI21 in the NIR and in the molecular bands. This is attributed to the different modelling of the red supergiants in both atmosphere models in the NIR, even though they are very similar in the optical model. At these ages, the contribution of red supergiant stars to the spectra of the population increases with the wavelength having a significant contribution in the NIR (see Cerviño & Mas-Hesse 1994).

For 100 Myr, the new models have a lower flux in the TiO molecular bands of the NIR than MI21. This is caused by the new stellar atmosphere models of PHOENIX for the same reasons as for 10 Myr, but more focused in the molecular bands. PHOENIX spectra have higher opacities than the C14 models, and thus their spectra in that region are less luminous in that wavelength range. Moreover, the PHOENIX stellar library has a

Table 4. Magnitudes in broad-band filters of the SSPs models.

IMF	Z	$\log t$	U	B	V	R	u	g	r	i	z
CHA	0.02	5.00	−0.340	0.674	0.905	1.031	0.773	1.122	1.559	1.967	2.247
CHA	0.02	5.48	−0.380	0.635	0.868	0.995	0.732	1.084	1.522	1.931	2.213
CHA	0.02	5.70	−0.422	0.594	0.826	0.953	0.691	1.044	1.480	1.889	2.171
CHA	0.02	5.85	−0.465	0.550	0.781	0.907	0.647	0.999	1.435	1.843	2.124
CHA	0.02	6.00	−0.526	0.493	0.726	0.853	0.586	0.943	1.380	1.789	2.071
CHA	0.02	6.10	−0.635	0.387	0.619	0.745	0.477	0.836	1.273	1.682	1.964

Notes. Column 1 shows the IMF, column 2 corresponds to the stellar metallicity of the SSP, and column 3 is the age. Columns 4 to 7 are the Johnson-Cousins-Glass system magnitudes U, B, V, and R in the Vega system, while columns 8–12 refer to the magnitudes u, g, r, i, and z for the SDSS filters AB system. The whole table is available at the CDS.

better coverage of $T_{\rm eff}$ in the H-R diagram, by actually including stars as cold as 2300 K, whereas in C14 the coolest star is 3300 K. This is especially relevant for intermediate and old ages, since there is a significant fraction of stars cooler than 3300 K.

Finally, for the 1 Gyr and 10 Gyr ages, there are two main differences between the new models and MI21. In the bluer part of the spectra, the new models have less flux in the G band area, ~4300 Å, more prominent for 10 Gyr than for 1 Gyr. This is caused by the different modelling of the CH molecular absorption bands in the C14 and PHOENIX libraries.

3.2. Derived properties

3.2.1. Magnitudes and colours

We also computed some magnitudes in bands that are within our wavelength range: U, B, V, and R in the Johnson system and u, g, r, i, and z in the SDSS system. In Table 4 we give these magnitudes for all ages, metallicities, and IMFs at the CDS. Here we show as an example the values for six ages, solar metallicity, and the CHA IMF. The evolution of the nine magnitudes is shown in Fig. 4, with a magnitude in each panel, as labelled.

There are differences between the old and the new models versions for all magnitudes. For young ages, the magnitudes of the new models are 0.04–0.06 dex higher, and thus less luminous than MI21. Then, the new models magnitudes decrease until they reach a maximum difference at around at 2–3 Myr; that is, 0.12 dex smaller than MI21 for redder (R, r, i, and z) bands and 0.09 dex smaller than MI21 for the bluer (U, B, V, u, and g) ones, respectively. Then, both models are very similar until they reach ages of around 100 Myr, when the new models have smaller magnitudes than MI21, around 0.03 dex, for the blue and bigger magnitudes than MI21, also around 0.03, for the red magnitudes.

3.2.2. 4000 Å break

We also compared the indices D4000 (Bruzual 1983) and Dn4000 (Balogh et al. 1999; Kauffmann et al. 2003) of the 4000 Å break, which are known to be proxies of the age of the stellar population. In Fig. 5, we show the comparison for $Z = 0.02$ between MI21 and the present work models. In general, the models agree very well, except in two age ranges: 1) 10–30 Myr, where the newest models are 2% smaller than the MI21 one; and 2) when the age is older than 4 Gyr, where the newest models are 3.5% higher than the previous ones in the case of Dn4000. In both cases, the difference is due to the cool stars' spectral libraries used for them, C14 for MI21 and PHOENIX in this work, which have small differences in the area before the break – mainly in the CN band 3883 area – that could be attributed to the modelling of the molecular lines done in each atmosphere model. The comparison for $Z = 0.004$ is in 5. The general trends of both libraries are maintained by using the MUN05 +PHOENIX+new PoWR models. The difference in the D4000 index does not have a great effect on estimating the age using the new D4000 breaks.

3.3. Calcium triplet

We also compared the calcium triplet (CaT) indices using the continuum definition of Cenarro et al. (2001) and the line definition of García-Vargas et al. (2020). The comparison between the new models and MI21 for $Z = 0.02$ is shown in Fig. 6. For the youngest ages (0.1–10 Myr), the new models have higher values than the old ones, with the biggest difference at the peak at 10 Myr with a difference of 20%. In the ages from 10 Myr to 100 Myr, the CaT of the new models is smaller than for the MI21 models. This is especially significant for the ages around 20 Myr (log(age) = 7.3). In the case of intermediate ages of between 100 Myr and 1 Gyr, the CaT indexes of the new models are slightly higher, by ~3%, than the ones of the old models. Finally, for ages older than 1 Gyr, the CaT of the new models have smaller values than the ones of the MI21 models, with a maximum difference in that age range of ~7%.

The differences in the CaT are caused by the change in the new PoWR models for the young ages with a secondary contribution, especially for ages between 10 and 30 Myr, of the change from C14 atmospheres to the PHOENIX atmospheres for red supergiants. The comparison for the lowest metallicity is shown in Appendix A.3.

3.4. Comparison with other SSP models

We compared our new models with other stellar population synthesis models, both theoretical, CBC20, and empirical, E-MILES, MaStar (Ma20), and XSL. For XSL and E-MILES, we used the models computed with the Padova 2000 isochrones to make a more similar comparison and see only the effects of the stellar libraries. We compared the models of solar metallicity for 100 Myr, 1 Gyr, and 10 Gyr. We normalised all the spectra to a 10 Å band around 5500 Å, where there is no prominent feature. The comparison of the models is shown in Fig. 7. All models agree in the optical region, except for CBC20, which has lower fluxes in the red part. However, in the NIR each model has a very different spectrum.

For 100 Myr, E-MILES and our models agree until ~9000 Å, at which point E-MILES models suddenly drop whereas our

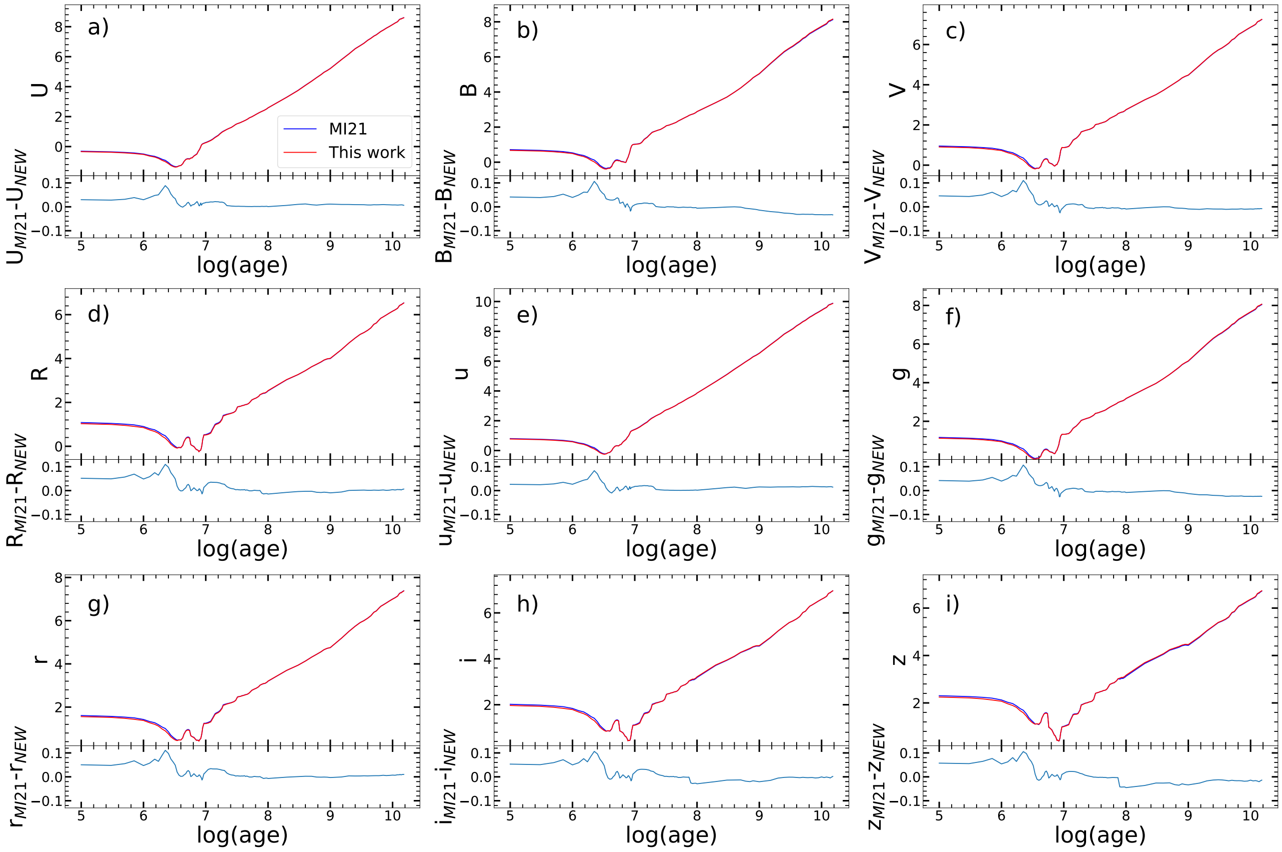

Fig. 4. Evolution of magnitudes a) U, b) B, c) V, d) R, e) u, f) g, g) r, h) i, and i) z with age: comparison of results between MI21, blue, and this work, red, with residuals in the bottom panel for CHA IMF and $Z = 0.02$.

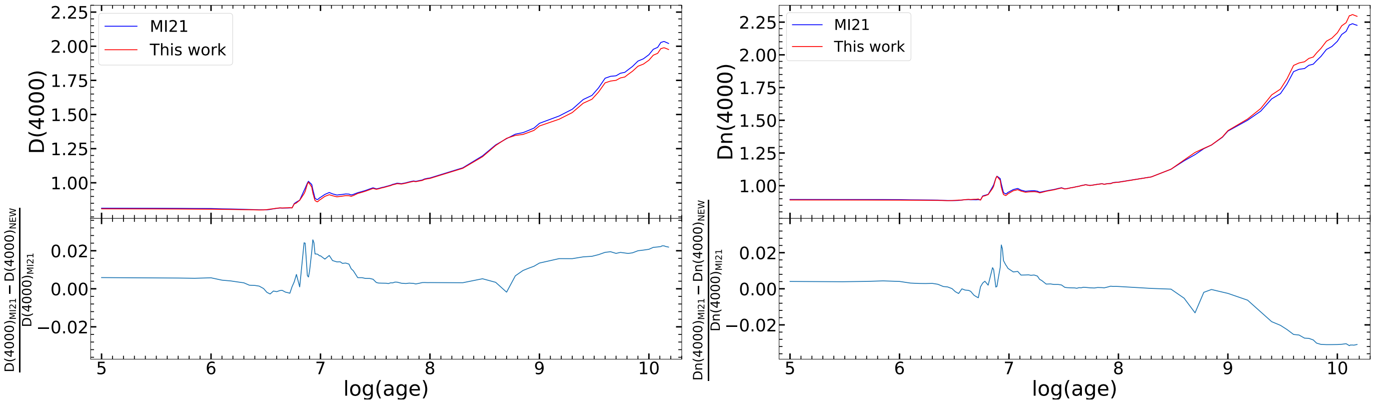

Fig. 5. D4000 and Dn4000 break time evolution comparison between MI21 (blue line) and this work (red line) for $Z = 0.02$.

models decrease slowly. MaStar models have lower fluxes in the NIR than the rest of the models.

In the case of 1 Gyr, XSL has the highest fluxes and very strong molecular bands in the NIR. E-MILES has smaller fluxes in the NIR in general and in the TiO molecular band around 8600 Å in particular. Our models are similar to those of E-MILES until ~8800,Å, at which point our models start to have lower fluxes than those of E-MILES. Finally, MaStar has fluxes lower than those of the rest of the models.

Finally, for 10 Gyr, XSL, E-MILES and our models have similar fluxes. However, in the region 8800–9100 Å our models have slightly lower fluxes than XSL and E-MILES.

The differences between XSL and E-MILES compared with our models are mostly attributed to the different libraries they include, since the same isochrones are used for the models. However, the differences with MaStar models could also be due to the fact that they are using a different algorithm, and different stellar tracks (the Geneva group tracks Ekström et al. 2012).

4. Analysis of stellar populations of low-metallicity systems

4.1. High-resolution observations of the globular cluster M15

After quantifying the difference between the models from MI21 and the new ones of this work, we tested the new models with

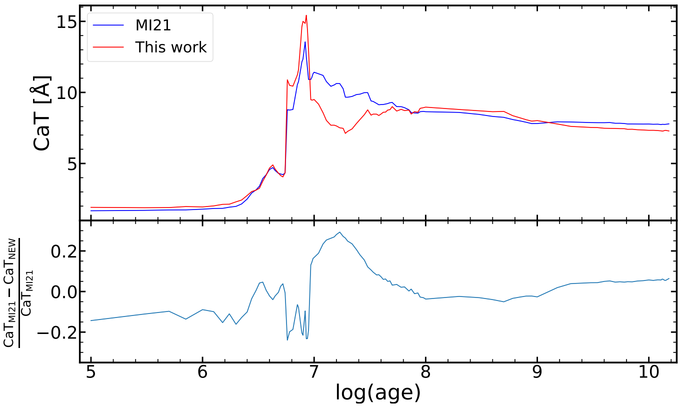

Fig. 6. Calcium triplet time evolution comparison for between MI21 (blue line) and this work (red line) for $Z = 0.02$.

observations that have a similar spectral resolution. Similarly to the analysis performed in MI21, we analysed the spectra of the globular cluster M15, which is a classical example of an old and metal-poor stellar population.

In order to do so, we used the spectrum of the globular cluster M15, observed with MEGARA in the HR-I set-up (see MI21 for more specific details). This spectrum has very high signal-to-noise ratio (S/N) in the CaT area (~100 S/N per Å). We used a χ^2 method to find the best model that fits the observed spectrum and we obtained an age of $\tau = 12.8$ Gyr and a metallicity of $Z = 0.0004$, which corresponds to $\log(Z/Z_\odot) = -1.7$, by using the solar abundance of $Z_\odot = 0.02$ (Grevesse & Sauval 1998). These results are better estimates than the ones obtained in MI21, with $\chi^2_{\mathrm{new}} = 5.14$, smaller than the $\chi^2_{\mathrm{old}} = 6.54$. Moreover, the new results are closer to recent estimates from the literature by O'Malley et al. (2017), who found $\tau = 12.5 \pm 1.3$ Gyr and [Fe/H] = −2.33, obtained by analysing colour magnitude diagrams with *GAIA* data of key stars in the globular cluster. In the previously fitted model, there were too many metallic lines that could not be found in the observed spectrum even with the lowest metallicity modelled in MI21, $Z = 0.004$, whereas the new model better fits these observed features in the spectrum. This shows the great advantage of having low-metallicity models available, which enable us to reproduce these kinds of systems. We present the new best-fitting model in Fig. 8, where the observed spectrum is shown with the red line, while the best-fitting model, corresponding to the indicated parameters, is the blue line.

4.2. Analysis of the stellar populations of dwarf galaxies

We used these new models to analyse the stellar populations of dwarf galaxies in which the low-metallicity stars make a significant contribution to the total stellar population. Dwarf galaxies have a wide range of morphological types, SFHs, and so on. However, they generally have lower metallicities than normal massive galaxies. Therefore, they are ideal examples for seeing the capabilities of the new generation of low-metallicity SSPs for the analysis of stellar populations. In this case, we chose the dwarf galaxies observed by MaNGA (Bundy et al. 2015) that were studied in the MaNDALA Value Added Catalogue (Cano-Díaz et al. 2022). These galaxies were selected to have stellar masses lower than $\log M(\mathrm{M}_\odot) < 9.1$. These observations have good coverage in the wavelength range of [3650 Å–10 300 Å] with $R \sim 2100$.

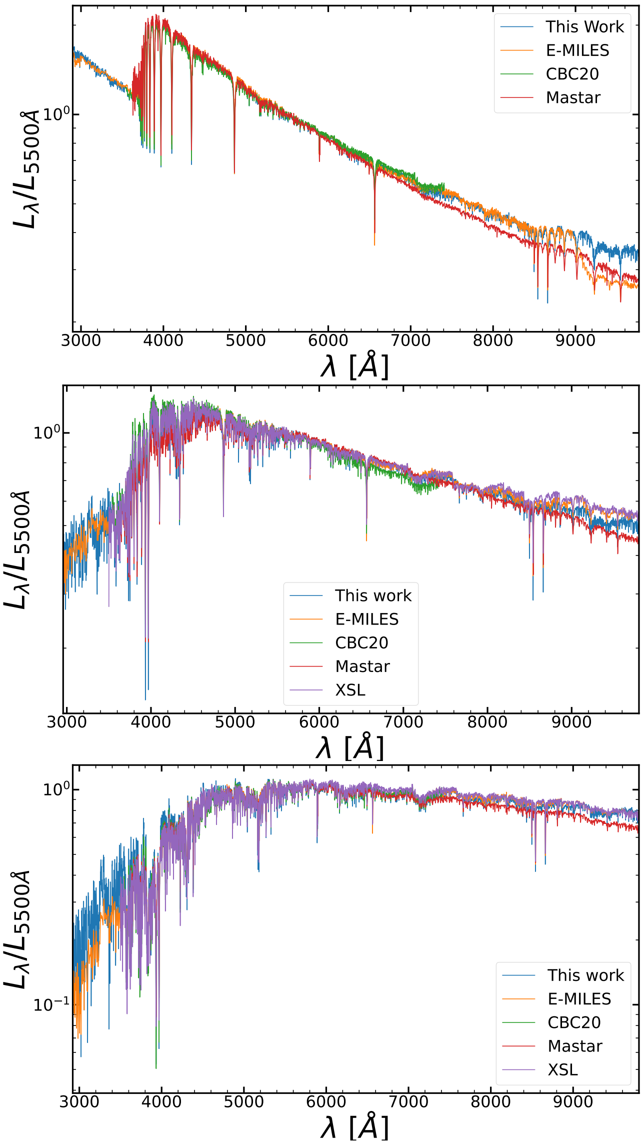

Fig. 7. Comparison of E-MILES (orange), CBC20 (green), MaStar (red), XSL (purple), and our new models (blue) for solar metallicity and 100 Myr, left, 1 Gyr, centre, and 10 Gyr, right.

We extracted the spectra of the 131 galaxies, adding the spaxels of the IFU up to 1 effective radius, R_e. Then, we made a selection cut of the spectra based on the criteria of having a S/N greater than 6 in the H_α, H_β, H_γ, Mg I b triplet region and the CaT region. After applying the S/N cut, we obtained a total of 31 galaxies from the original sample. We analysed all the observed galaxy spectra using the full spectral fitting code FADO (Gomes & Papaderos 2018) and the newly computed SSP using the CHA IMF. FADO has already been tested with the previous version of HR-PYPOPSTAR in MI21. During the analysis, we masked the region around 5570 Å to avoid the contamination from telluric lines. Regarding the full spectral fitting analysis, we ran the code ten times with different random initial seeds for each galaxy, in order to avoid local minima in the final solution, and we averaged over the different runs. In Fig. 9, we show an example of one of the fit for one of the dwarf galaxies from FADO.

In addition to the star formation and chemical enrichment history, FADO gives as outputs the mean stellar age, mean stellar metallicity (both weighted by mass and light), and the total

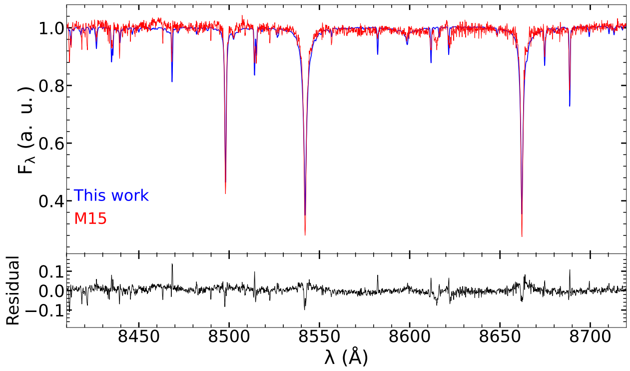

Fig. 8. Spectra of M15 from MEGARA observations in red, and the best model from HR-PyPopStar fitting the data in blue.

Table 5. Properties of the stellar populations of the sample obtained by FADO using the new SSP models.

MaNGA Id	log M_*	$\langle\log(\tau)\rangle_L$	$\langle\log(\tau)\rangle_M$	$\langle\log(Z/Z_\odot)\rangle_L$	$\langle\log(Z/Z_\odot)\rangle_M$
7815-6101	9.11	8.58	9.66	−0.29	−0.41
7992-12703	8.75	8.44	9.17	−0.36	−0.27
8135-6101	8.42	8.62	9.51	−0.38	−0.23
8150-3701	6.77	8.03	9.61	−0.64	−0.86
8152-12702	8.14	9.01	9.58	−1.01	−1.26
8449-6101	8.83	8.11	8.93	−0.29	−0.29

Notes. Column 1 is the MaNGA Id, column 2 corresponds to the stellar mass, columns 3 and 4 are the mean stellar age weighted by mass and light and columns 5 and 6 are the mean stellar metallicity weighted by mass and light. The whole table is available at the CDS.

formed and current stellar masses. In Table 4, we summarise the averaged values of the stellar population properties of the galaxies obtained from the full spectral fitting. The whole table is available at the CDS.

After computing the mean stellar metallicities and stellar masses, we considered the mass-mean metallicity and the mass-mean age relations of the galaxies in the sample. Several works have tried to explore the mass-metallicity relation of dwarf galaxies in the past using different methods and subsamples. Some of the works devoted to studying all the galaxies also traced at least part of the range of dwarf galaxies. Thus, Gallazzi et al. (2005) analysed up to 200 000 galaxies from the SDSS DR2 survey (Abazajian et al. 2004) using spectral indices sensitive to age and metallicity and reconstructing the SFHs of the galaxies, Panter et al. (2008) used 300 000 galaxies from the SDSS DR3 (Abazajian et al. 2005) using a similar analysis than the one from Gallazzi et al. (2005) to reconstruct the SFH of the galaxies, Kirby et al. (2013) studied red giants in local dwarf spheroidal and irregular dwarf galaxies in the Local Group using indices to obtain the mean age and metallicity of these dwarf galaxies, Kudritzki et al. (2016) studied blue supergiant stars in several Local Group dwarf galaxies using low-spectral-resolution spectra, Zahid et al. (2017) stacked the spectra of 90 000 star-forming galaxies from SDSS DR7, DR10, and DR11 (Abazajian et al. 2009; Alam et al. 2015) in different stellar mass bins, creating combinations of star formation bursts and chemical evolution models to fit the stellar absorption lines, and more recently Sextl et al. (2023) performed a similar work to Zahid et al. (2017) but distinguished between star-forming galaxies, passive galaxies, and a third group that considers all of the galaxies, in order to find the mass-metallicity relation of these three groups. In general, there are hints that star-forming dwarf galaxies have higher metallicities on average than their passive counterparts.

In Fig. 10, we show our results for the current stellar mass and the mean stellar metallicity weighted by light as blue dots. We have also binned the results with mass bins of 0.4 dex to show the trends of the results in a more comprehensive way. We compare our results with those found by Gallazzi et al. (2005), Panter et al. (2008), Kirby et al. (2013), Kudritzki et al. (2016), Zahid et al. (2017), Sextl et al. (2023).

Our results follow similar trends to Gallazzi et al. (2005) and Sextl et al. (2023) for the mean of all galaxies of SDSS, but our models have a slightly higher mean stellar metallicity weighted by light, $\langle Z\rangle_L$, than both of them. In particular, our models show values, $\langle Z\rangle_L$, between the sub-sample of SF and the mean of all galaxies from Sextl et al. (2023). Our models also have a similar mass-metallicity relation to studies of local star-forming galaxies by Kudritzki et al. (2016) and Zahid et al. (2017). The star-forming galaxies tend to show higher $\langle Z\rangle_L$ than other works done with dwarf spheroidals (Kirby et al. 2013), or take all the dwarf galaxies as a whole such as Gallazzi et al. (2005), Panter et al. (2008). In fact, Sextl et al. (2023) showed that star-forming galaxies tend to have higher $\langle Z\rangle_L$ than the non-star-forming galaxies. Regarding our sample, 29 of 31 galaxies, 93.5% of the ones in the sample, are star-forming galaxies.

4.3. Comparisons with MaNDALA Value Added Catalogue

Finally, we made a direct comparison of our results of the 31 analysed dwarf galaxies and the results obtained by Cano-Díaz et al. (2022, hereinafter CD22) for the same sample. In Fig. 11, panel a) we show the comparison of the results of the analysis within 1 R_e from CD22 and this work of the mean stellar metallicity weighted by light versus the current stellar mass. We also show the binned results using bins of 0.4 dex. Our models have a slightly higher $\langle Z\rangle_L$ than CD22 for the same mass bin, but both models agree within the error bars, except for the bin of the highest mass, for which our models clearly have more metallicity, $\langle Z\rangle_L$, than CD22. In general, our models have an increasing $\langle Z\rangle_L$ with increasing mass, whereas CD22 has no trend of $\langle Z\rangle_L$.

Similarly, in panel b), we show the relation between the mean age weighted by light and the stellar mass and the binned results using the same stellar mass bins as in panel a). We find younger ages, $\langle\log(\tau)\rangle_L$, than CD22 for the highest mass and older ages, $\langle\log(\tau)\rangle_L$, than CD22 for the low stellar masses. Our analysis shows a small trend of a lower mean stellar age weighted by light, $\langle\log(\tau)\rangle_L$, for higher masses. On the contrary, CD22 does not find any trend of age, $\langle\log(\tau)\rangle_L$, with mass.

Finally, in Fig. 12 we show the age metallicity relation of these galaxies. In our results, there seem to be two distinct stellar populations: one predominantly young population that has a high mean stellar metallicity and another older stellar population with a lower mean stellar metallicity. In the case of CD22, they seem to have one cloud with similar properties of stellar populations for all galaxies.

This suggests that these new models could be useful to disentangle the age-metallicity degeneracy, and thus obtain more accurate estimates of the stellar population parameters. However, we have too few spectra of galaxies to have robust statistics, and more observations are necessary to come to any final conclusion.

These two distinct populations that we find in the age-metallicity relation have very different SFHs. On the one hand, the population of old age and low metallicities has SFHs with one or two star formation bursts a few gigayears ago, and star

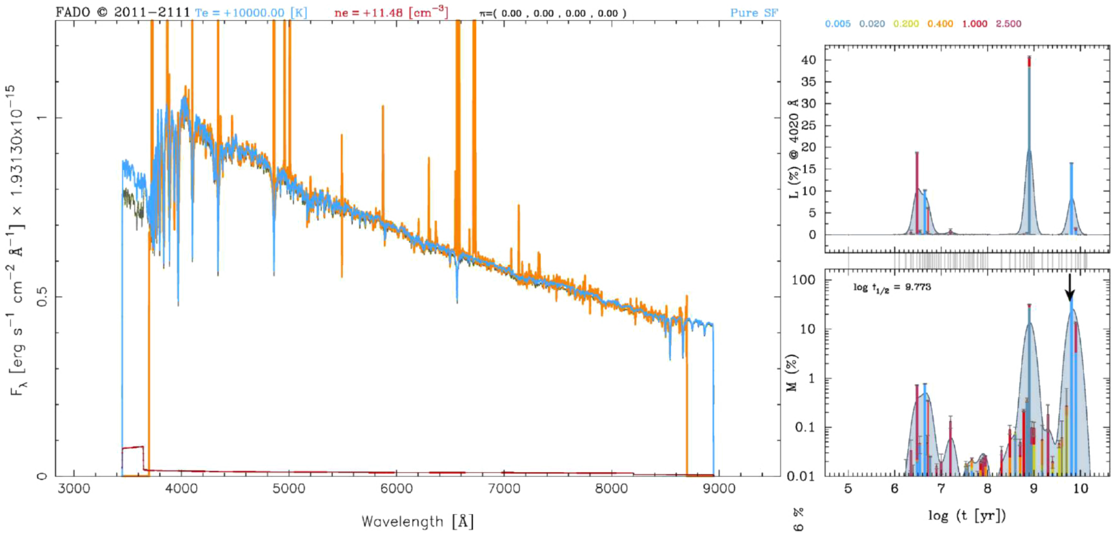

Fig. 9. Example of one of the full spectral fitting fits of FADO, of the dwarf galaxy 8596-6103. In the left plot, the orange line represents the observed spectra, the blue line the fitted stellar spectra, and the green line the fitted nebular continuum. The top right image shows the contribution of each SSP to the fit in luminosity at λ = 4020 Å. In the bottom right panel is the SFH of the galaxy given by the mass contribution of each SSP to the fit.

formation that stopped after that, so their star formation is now very low, the old and low-metallicity stellar population being the only population still present. However, the young-age and high-metallicity population group had a burst of intermediate age, followed by a recent burst, now showing a high star formation rate (SFR).

In order to show this difference in the SFH, we use the difference between the averaged by light and averaged by mass ages: $\langle\log(\tau)\rangle_M$ and $\langle\log(\tau)\rangle_L$. $\langle\log(\tau)\rangle_L$ is dominated by the youngest stellar populations, while $\langle\log(\tau)\rangle_M$ is dominated by the oldest stellar populations. Thus, the difference can be used as a tracer of how dispersed the star formation bursts are in time. If there have been recent star formation events, the difference between both quantities will be important, but if the star formation stopped long ago the difference will be insignificant. In Fig. 13, we show a) the $\langle\log(\tau)\rangle_L$ versus $\langle\log(\tau)\rangle_M - \langle\log(\tau)\rangle_L$ and b) the $\log(\langle Z\rangle_L)$ versus $\langle\log(\tau)\rangle_M - \langle\log(\tau)\rangle_L$. It can be observed that the low-metallicity and old age populations from Fig. 12 tend to have small values, $\langle\log(\tau)\rangle_M - \langle\log(\tau)\rangle_L$, so they have a very low fraction of a young stellar population. This implies that the SFR of the galaxies with just the old stellar population dropped heavily after the low-metallicity population was formed.

Sextl et al. (2023) also found that the proportion of young to old stars is higher in dwarf galaxies and depends strongly on the SFR. Moreover, they also found that the metallicity of the young stellar population is significantly higher than the one of old stellar population in low-mass systems in comparison with high-stellar-mass galaxies. This could explain the diversity in the properties of the stellar populations of the analysed dwarf galaxies.

There are differences in the mean stellar metallicity weighted by light and stellar mass relation, and mean stellar age weighted by light and the stellar mass relation of CD22 and this work. There could be several causes behind these differences: the different SSP models used, the different full spectral fitting codes used, and also the analysis method. First, the SSP models of CD22 and ours are different. CD22 used a version of the Bruzual and Charlot code (Charlot, in prep) that included the MaStar (Yan et al. 2019) stellar templates for cold stars and theoretical spectra (Leitherer et al. 2010) for hot stars, and they used the IMF of Salpeter (1955). We have shown in Section 3.4 that our models follow similar trends to other SSP models that use empirical libraries and very similar isochrones to our models, such as XSL and EMILES, except in the reddest part of the NIR, $\lambda > 9000$, but this region is excluded from the analysis. Thus, there should not be any systematic effect in our models.

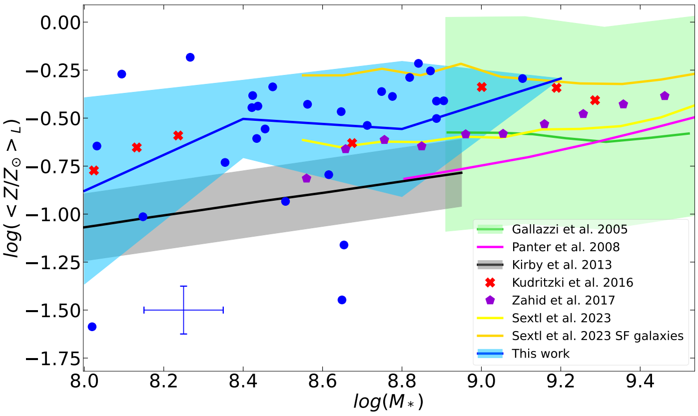

Fig. 10. Current stellar mass and mean stellar metallicity weighted by light relation. In blue circles are our result with the mean error at the bottom. The green line is from Gallazzi et al. (2005), the magenta line is from Panter et al. (2008), the black line is from Kirby et al. (2013), red Xs are from Kudritzki et al. (2016), violet pentagons are from Zahid et al. (2017), and the orange and yellow lines are the star-forming regions and the mean of all galaxies from Sextl et al. (2023). The blue dots are the results from our work and the blue cross at the bottom represents the mean error of our analysis.

Another possible cause of this difference is the full spectral fitting code used. We have used FADO, whereas CD22 used pyPipe3D. These two codes are very different and explore the parameter space in a very different way: FADO uses a genetic algorithm to make a random walk through the parameter space more efficiently, and pyPipe3D uses ‘non-lineal models’ to fit the extinction, the redshift, and the velocity dispersion and then analyses the parameter space. However, a full comparison of the effect of using a different full-spectral fitting code in the

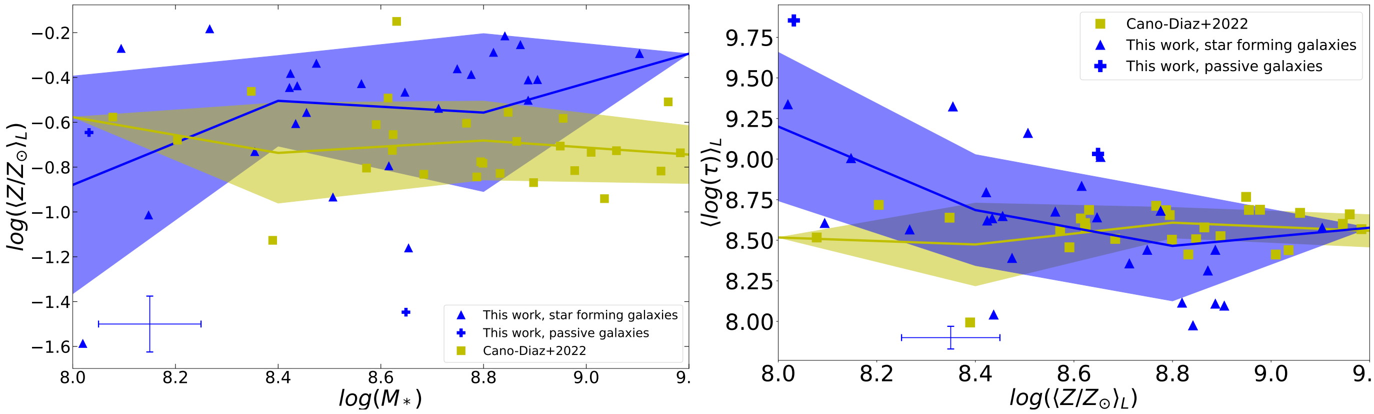

Fig. 11. Relation of a) the mean stellar metallicity as $\langle Z\rangle_L$ and b) the mean stellar age, as $\log\langle\tau\rangle_L$, vs the stellar mass as $\log M_*$. Green squares are the results from Cano-Díaz et al. (2022), blue triangles for star-forming galaxies and blue crosses for passive galaxies are the results from this work, and the blue cross in the bottom left shows the mean error of this work in stellar mass, mean stellar age, and mean stellar metallicity.

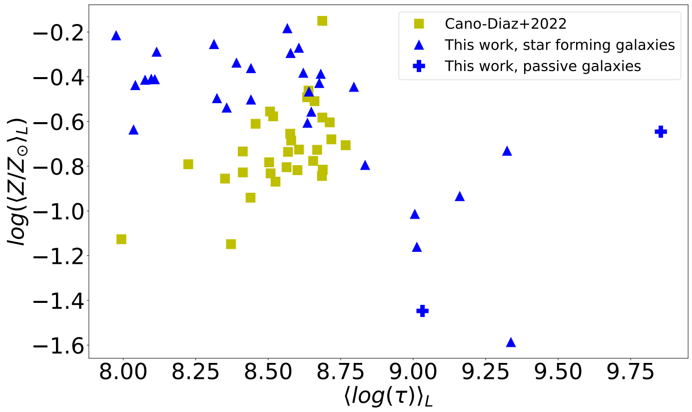

Fig. 12. Comparison of the mean of the age and the mean stellar metallicity of Cano-Díaz et al. (2022), green squares, and this work. Blue triangles represent star-forming galaxies and blue crosses passive galaxies.

analysis of the stellar populations is beyond the scope of this paper.

Finally, another possible cause of the difference is the analysis method. On the one hand, we stacked the spectra for 1 R_e, and then we analysed the resulting spectra to obtain the stellar properties at 1 R_e. On the other hand, CD22 created a map of the stellar population properties of the galaxy, by stacking the result of the map to obtain those properties. These two methods are not equivalent and given the low S/N of these systems some possible differences could arise when comparing their results.

5. Conclusions

We have made a new set of HR-PYPOPSTAR models with a wider range of metallicities, basically reaching lower metallicities than in our first version of the models. Using the stellar libraries from citetmun05, Husser et al. (2013) and the new version of PoWR models for O and B stars, a set of high-wavelength-resolution theoretical SEDs for SSPs from 2500 Å to 10 500 Å with a constant wavelength step of $\delta\lambda = 0.1$ Å has been computed. We used isochrones from the Padova group (Bressan et al. 1993; Fagotto et al. 1994a,b; Girardi et al. 1996) for 106 different ages in the range of $t = 0.1$ Myr to 15 Gyr, six metallicities, $Z = 0.0001$, 0.0004 0.004, 0.008, 0.02, and 0.05, and four IMFs from Salpeter (1955), Ferrini et al. (1990), Kroupa (2002 with exponent −2.7 for the massive star range), and Chabrier (2003).

We checked the effect of using these libraries by comparing the SEDs obtained by MI21 and the ones obtained in these new models for solar metallicity and CHA IMF. We found some differences, especially in the young ages, due to the update of the O and B stars from PoWR, and the old age populations, due to the use of the PHOENIX stellar spectra. Regarding the old population, the differences are especially visible in the NIR and in molecular bands, such as the G band and TiO bands, which is attributed to the use of this PHOENIX library for cool stars (in MI21 we used C14). The PHOENIX library has a more complete list of molecular lines and has spherical geometry instead of plane-parallel geometry, which better reproduces cool stars. Moreover, the temperature coverage of the HR diagram is more complete in the PHOENIX library.

The magnitudes remain similar in both old and new models, with average differences smaller than 0.06 dex, the highest difference being 0.12 dex for the youngest ages, where we have updated the models for O and B stars. We also checked the change in D4000 and Dn4000 for $Z = 0.02$ and CHA IMF, finding small differences in D4000 (the maximum difference is 2%) and in Dn4000 (the maximum difference is 3.5%), which are caused by the different modelling of the CN bands in the C14 and PHOENIX libraries.

We also compared our resulting SEDs with E-MILES, MaStar, CBC20, and XSL. For E-MILES and XSL, we chose the Padova00 isochrones that are very similar to the isochrones that we use. All models agree well in the optical, but each SSP model is different in the NIR. XSL, E-MILES, and our models agree on the continuum level, while each one has its own strength for the TiO molecular bands.

In order to test low-metallicity HR SSP models, we used our new models to analyse a different set of stellar population data. First, we analysed high-resolution data of the globular cluster M 15 using data from HR-I of MEGARA. We made an analysis of χ^2 to obtain the best estimate of the age and the metallicity. We found an older age and a lower metallicity than the previous results we found in Millán-Irigoyen et al. (2021). We found an age of $\tau = 12.8$ Gyr and the metallicity $Z = 0.0004$. These results are similar to other works from the literature that studied the same object using other techniques as this one from

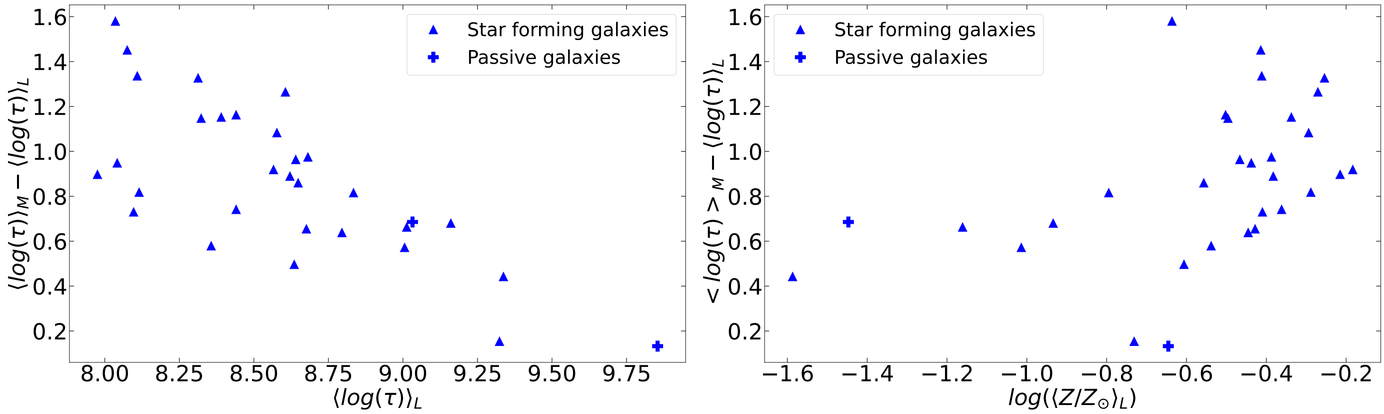

Fig. 13. Relation of the $\log\langle\tau\rangle_L - \log\langle\tau\rangle_M$ vs a) the mean stellar age weighted by light, as $\log\langle\tau\rangle_L$, and the mean stellar metallicity as $\log\langle Z\rangle_L$. The star-forming galaxies are represented by blue triangles and passive galaxies as blue crosses.

O'Malley et al. (2017), who found $\tau = 12.5 \pm 1.3$ Gyr and [Fe/H] = −2.33.

Finally, we analysed the stellar populations of dwarf galaxies from the MaNGA sample up to redshift 0.15, where the new low-metallicity models are expected to contribute significantly to their stellar content. After obtaining the spectra at $1\,R_e$, we made a selection of the spectra based on the S/N of key areas for the stellar population analysis, H_α, H_β, H_γ, the MgI b triplet region, and the CaT. After this cut, we obtained 31 galaxies, 29 star-forming ones and 2 passive ones, which were analysed using the full spectral fitting code FADO with the new models and the CHA IMF. We ran the analysis ten times to avoid false minimum solutions and produced a mean of all the results.

We compared the current stellar masses and mean stellar metallicity, weighted by light, with other studies from the literature. Our results follow trends similar to ones in other works that analysed star-forming galaxies (Kudritzki et al. 2016; Zahid et al. 2017; Sextl et al. 2023) and have a slightly higher mean stellar metallicity weighted by light, but are within the error bars of those studies (Gallazzi et al. 2005; Sextl et al. 2023). We also made a direct comparison of our results with those obtained by Cano-Díaz et al. (2022) for the same galaxies. In the case of the current stellar mass–mean stellar metallicity relation, our $\langle Z\rangle_L$ is higher than CD22 for the same mass bin, but both models agree within error bars, except for the highest mass bin.

In the case of the current stellar mass–mean stellar age relation, our results in the lowest mass bin have higher $\langle\log(\tau)\rangle_L$ than CD22 and have smaller $\langle\log(\tau)\rangle_L$ than CD22 for higher stellar masses. We find a small trend of lower mean stellar age weighted by light for higher masses, while CD22 found no trend with stellar mass.

Then, we compared the age-metallicity relation. We found two different stellar populations: one with low $\langle\log(\tau)\rangle_L$ and high $\langle Z\rangle_L$ and a second one with high $\langle\log(\tau)\rangle_L$ and low $\langle Z\rangle_L$. These two populations seem to have completely different SFHs: the low $\langle\log(\tau)\rangle_L$ and high $\langle Z\rangle_L$ galaxies had a burst 100–500 Myr ago followed by a very recent burst and have a high present-day star formation; while the high $\langle\log(\tau)\rangle_L$ – low $\langle Z\rangle_L$ galaxies had one or two bursts 3–4 Gyr ago and their star formation rate is now very low, so the majority of the population is old-age and low-metallicity. However, the size of the sample is too small to draw any definitive conclusion and it would be necessary to have a more complete and high-S/N spectral sample of dwarf galaxies.

Finally, we evaluated the possible causes of the different results between CD22 and our work. We have identified three possible causes: the difference in SSP models, the full-spectral fitting code used, and the method of analysing the data.

Data availability

Tables4 and5 are available at the CDS via `https://cdsarc.cds.unistra.fr/viz-bin/cat/J/A+A/704/A322`. The computed SEDs and the tables with the magnitudes, are available on the web page: `http://www.pypopstar.com`. The user are available to download the complete set of models or a required subset (with all ages) just selecting by IMF and Z.

Acknowledgements. I.M.-I. wants to thank Guinevere Kauffmann for the helpful comments and discussion that helped to improve the paper. The authors would like to thank the anonymous referee who provided useful and detailed comments on an earlier version of the manuscript. This research has been funded by grant PID2019-107408GB-C41 and PID2022-136598NB-C33 funded by MCIN/AEI/10.13039/501100011033 and by "ERDF A way of making Europe". Funding for the Sloan Digital Sky Survey IV has been provided by the Alfred P. Sloan Foundation, the U.S. Department of Energy Office of Science, and the Participating Institutions. SDSS acknowledges support and resources from the Center for High-Performance Computing at the University of Utah. The SDSS web site is `www.sdss4.org`. SDSS is managed by the Astrophysical Research Consortium for the Participating Institutions of the SDSS Collaboration including the Brazilian Participation Group, the Carnegie Institution for Science, Carnegie Mellon University, Center for Astrophysics | Harvard & Smithsonian (CfA), the Chilean Participation Group, the French Participation Group, Instituto de Astrofísica de Canarias, The Johns Hopkins University, Kavli Institute for the Physics and Mathematics of the Universe (IPMU)/University of Tokyo, the Korean Participation Group, Lawrence Berkeley National Laboratory, Leibniz Institut für Astrophysik Potsdam (AIP), Max-Planck-Institut für Astronomie (MPIA Heidelberg), Max-Planck-Institut für Astrophysik (MPA Garching), Max-Planck-Institut für Extraterrestrische Physik (MPE), National Astronomical Observatories of China, New Mexico State University, New York University, University of Notre Dame, Observatório Nacional/MCTI, The Ohio State University, Pennsylvania State University, Shanghai Astronomical Observatory, United Kingdom Participation Group, Universidad Nacional Autónoma de México, University of Arizona, University of Colorado Boulder, University of Oxford, University of Portsmouth, University of Utah, University of Virginia, University of Washington, University of Wisconsin, Vanderbilt University, and Yale University.

References

Abazajian, K., Adelman-McCarthy, J. K., Agüeros, M. A., et al. 2004, AJ, 128, 502
Abazajian, K., Adelman-McCarthy, J. K., Agüeros, M. A., et al. 2005, AJ, 129, 1755
Abazajian, K. N., Adelman-McCarthy, J. K., Agüeros, M. A., et al. 2009, ApJS, 182, 543

Alam, S., Albareti, F. D., Allende, Prieto C., et al. 2015, ApJS, 219, 12
Balogh, M. L., Morris, S. L., Yee, H. K. C., Carlberg, R. G., & Ellingson, E. 1999, ApJ, 527, 54
Bressan, A., Bertelli, G., & Chiosi, C. 1993, LNP, 416, 352
Bruzual, A. G. 1983, ApJ, 273, 105
Bruzual, G., & Charlot, S. 2003, MNRAS, 344, 1000
Bundy, K., Bershady, M. A., Law, D. R., et al. 2015, ApJ, 798, 7
Cano-Díaz, M., Hernández-Toledo, H. M., Rodríguez-Puebla, A., et al. 2022, AJ, 164, 127
Cappellari, M. 2017, MNRAS, 466, 798
Cappellari, M., & Emsellem, E. 2004, PASP, 116, 138
Cenarro, A. J., Cardiel, N., Gorgas, J., et al. 2001, MNRAS, 326, 959
Cerviño, M., & Mas-Hesse, J. M. 1994, A&A, 284, 749
Chabrier, G. 2003, ApJ, 586, L133
Cid Fernandes, R., Mateus, A., Sodré, L., Stasińska, G., & Gomes, J. M. 2005, MNRAS, 358, 363
Coelho, P. R. T. 2014, MNRAS, 440, 1027
Coelho, P., Bruzual, G., Charlot, S., et al. 2007, MNRAS, 382, 498
Coelho, P. R. T., Bruzual, G., & Charlot, S. 2020, MNRAS, 491, 2025
Conroy, C., & van Dokkum, P. 2012, ApJ, 747, 69
Conroy, C., Gunn, J. E., & White, M. 2009, ApJ, 699, 486
Conroy, C., Villaume, A., van Dokkum, P. G., & Lind, K. 2018, ApJ, 854, 139
DESI Collaboration (Abdul-Karim, M., et al.) 2025, arXiv e-prints [arXiv:2503.14745]
Ekström, S., Georgy, C., Eggenberger, P., et al. 2012, A&A, 537, A146
Eldridge, J. J., & Stanway, E. R. 2009, MNRAS, 400, 1019
Fagotto, F., Bressan, A., Bertelli, G., & Chiosi, C. 1994a, A&AS, 104, 365
Fagotto, F., Bressan, A., Bertelli, G., & Chiosi, C. 1994b, A&AS, 105, 29
Ferrini, F., Penco, U., & Palla, F. 1990, A&A, 231, 391
Fioc, M., & Rocca-Volmerange, B. 1997, A&A, 500, 507
Fioc, M., & Rocca-Volmerange, B. 2019, A&A, 623, A143
Fritze-v. Alvensleben, U., & Bicker, J. 2006, A&A, 454, 67
Gaia Collaboration (Gallazzi, A., et al.) 2018, A&A, 616, A1
Gallazzi, A., Charlot, S., Brinchmann, J., White, S. D. M., & Tremonti, C. A. 2005, MNRAS, 362, 41
Garcia, Vargas M., & L., Diaz A. I., 1994, ApJS, 91, 553
García-Vargas, M. L., Bressan, A., & Díaz, A. I. 1995, A&AS, 112, 13
García-Vargas, M. L., Mollá, M., & Bressan, A. 1998, A&AS, 130, 513
García-Vargas, M. L., Mollá, M., & Martín-Manjón, M. L. 2013, MNRAS, 432, 2746
García-Vargas, M. L., Carrasco, E., Mollá, M., et al. 2020, MNRAS, 493, 871
Girardi, L., Bressan, A., Chiosi, C., Bertelli, G., & Nasi, E. 1996, A&AS, 117, 113
Gomes, J. M., & Papaderos, P. 2018, A&A, 618, C3
González Delgado, R. M., Cerviño, M., Martins, L. P., Leitherer, C., & Hauschildt, P. H. 2005, MNRAS, 357, 945
Grevesse, N., & Sauval, A. J. 1998, Space Sci. Rev., 85, 161
Husser, T.-O., Wende-von Berg, S., Dreizler, S., et al. 2013, A&A, 553, A6
Kauffmann, G., Heckman, T. M., White, S. D. M., et al. 2003, MNRAS, 341, 33
Kirby, E. N., Cohen, J. G., Guhathakurta, P., et al. 2013, ApJ, 779, 102
Kodama, T., & Arimoto, N. 1997, A&A, 320, 41
Kroupa, P. 2002, Science, 295, 82
Kudritzki, R. P., Castro, N., Urbaneja, M. A., et al. 2016, ApJ, 829, 70
Kurucz, R. L. 2013, Astrophysics Source Code Library [record ascl:1303.024]
Le Borgne, D., Rocca-Volmerange, B., Prugniel, P., et al. 2004, A&A, 425, 881
Leitherer, C., Schaerer, D., Goldader, J. D., et al. 1999, ApJS, 123, 3
Leitherer, C., Ortiz Otálvaro, P. A., Bresolin, F., et al. 2010, ApJS, 189, 309
Leitherer, C., Ekström, S., Meynet, G., et al. 2014, ApJS, 212, 14
Mancone, C. L., & Gonzalez, A. H. 2012, PASP, 124, 606
Maraston, C. 2005, MNRAS, 362, 799
Maraston, C., & Strömbäck, G. 2011, MNRAS, 418, 2785
Maraston, C., Strömbäck, G., Thomas, D., Wake, D. A., & Nichol, R. C. 2009, MNRAS, 394, L107
Maraston, C., Hill, L., Thomas, D., et al. 2020, MNRAS, 496, 2962
Martín-Manjón, M. L., García-Vargas, M. L., Mollá, M., & Díaz, A. I. 2010, MNRAS, 403, 2012
Millán-Irigoyen, I., Mollá, M., & Ascasibar, Y. 2020, MNRAS, 494, 146
Millán-Irigoyen, I., Mollá, M., Cerviño, M., et al. 2021, MNRAS, 506, 4781
Mollá, M. 2014, Adv. Astron., 2014, 162949
Mollá, M., García-Vargas, M. L., & Bressan, A. 2009, MNRAS, 398, 451
Munari, U., Sordo, R., Castelli, F., & Zwitter, T. 2005, A&A, 442, 1127
O'Malley, E. M., Gilligan, C., & Chaboyer, B. 2017, ApJ, 838, 162
Panter, B., Jimenez, R., Heavens, A. F., & Charlot, S. 2008, MNRAS, 391, 1117
Percival, S. M., Salaris, M., Cassisi, S., & Pietrinferni, A. 2009, ApJ, 690, 427
Rauch, T. 2003, A&A, 403, 709
Salpeter, E. E. 1955, ApJ, 121, 161
Sánchez, S. F., Pérez, E., Sánchez-Blázquez, P., et al. 2016a, RMxAA, 52, 21
Sánchez, S. F., Pérez, E., Sánchez-Blázquez, P., et al. 2016b, RMxAA, 52, 171
Sextl, E., Kudritzki, R.-P., Zahid, H. J., & Ho, I.-T. 2023, ApJ, 949, 60
Tojeiro, R., Heavens, A. F., Jimenez, R., & Panter, B. 2007, MNRAS, 381, 1252
Vazdekis, A., Coelho, P., Cassisi, S., et al. 2015, MNRAS, 449, 1177
Vazdekis, A., Koleva, M., Ricciardelli, E., Röck, B., & Falcón-Barroso, J. 2016, MNRAS, 463, 3409
Verro, K., Trager, S. C., Peletier, R. F., et al. 2022, A&A, 661, A50
Vink, J. S., de Koter, A., & Lamers, H. J. G. L. M. 2001, A&A, 369, 574
Wilkinson, D. M., Maraston, C., Goddard, D., et al. 2017, MNRAS, 472, 4297
Yan, R., Chen, Y., Lazarz, D., et al. 2019, ApJ, 883, 175
Zahid, H. J., Kudritzki, R.-P., Conroy, C., Andrews, B., & Ho, I.-T. 2017, ApJ, 847, 18

Appendix A: Comparison of spectra and properties at $Z = 0.004$

A.1. Comparison of spectra

We compared the spectra of MI21 and the new models for CHA IMF, $Z = 0.004$ and the ages 1, 10, 100, 1000 and 10000 Myr in Fig. A.1.

In the case of the young ages 1 and 10 Myr, the new models have 1.5% and 0.5% more luminosity than the MI21 and have higher absorption in the lines of the Balmer series. As in $Z = 0.02$, these changes are caused by the new models of the O and B stars from PoWR. For 100 Myr, the new models and MI21 are very similar. For 100 Myr the models are very similar with very small differences in some lines. In the case of 1 Gyr, the new models have stronger flux in the TiO and G-Band molecular bands. Finally, for the age of 10 Gyr, our new models have less flux in the G-Band than the previous models.

The causes for the differences are the same as in Z=0.02 the change in the stellar libraries, specially the change of C14 to PHOENIX for cool stars and the update of the PoWR O and B stars. In general, the differences found at Z=0.02 are maintained at Z=0.004, but these differences are smaller at Z=0.004 than at Z=0.02.

A.2. D4000 breaks

We have made a comparison of the D4000 and Dn4000 for the lowest metallicity that both models share, $Z = 0.004$. In the case of the D4000, the new results are 0.5% smaller than the ones in MI21 for all ages. In the case of Dn4000, the new models have smaller Dn4000 than MI21 for young ages, but they have higher Dn4000s than MI21 for ages than 4 Gyr with a maximum difference of 2.8%. The general trends of both D4000 and Dn4000 breaks observed for $Z = 0.02$ are maintained for $Z = 0.004$.

A.3. Calcium triplet

We compared the CaT for the lowest metallicity that both models share, Z = 0.004. The differences between the MI21 and the new models for the CaT are significantly smaller than the solar metallicity case, but they still have differences. For young ages 0.1 Myr to 1 Myr the new models have smaller CaT than the MI21 models with approximately 4%. For 1 Myr to 500 Myr (log(age)=8.7), the new models have higher CaT than the old ones with a maximum peak of $\sim$ 20% difference at 9 Myr. In the case of ages older than 500 Myr, the new models have smaller CaT than the ones from the MI21 models with a maximum difference of $\sim$ 7% for the oldest age.

A.4. Magnitudes

We compared the magnitudes between MI21 and this work in the bands: U, B, V and R, in the Johnson system and u, g, r, i and z in the SDSS system. The evolution of the 9 magnitudes is shown in Fig. A.4.

In general, the differences between MI21 and the new models at Z=0.004 is very small around 0.02 dex except for i and z magnitudes where the new models have 0.04 dex higher than the MI21 for the 200 Myr old population.

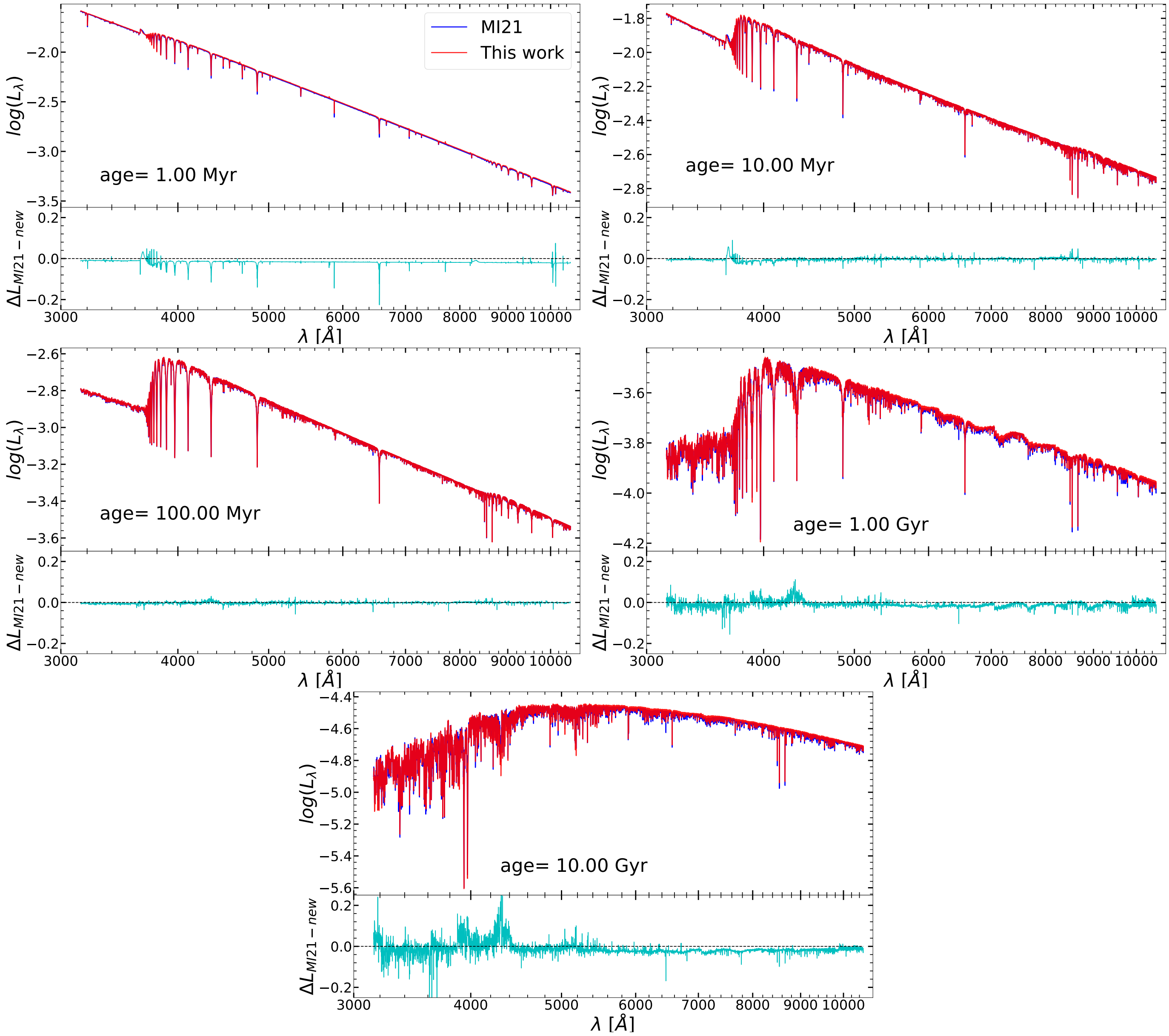

Fig. A.1. Comparison between the old version of HR-pyPopStar using the stellar library of C14 (MI21), in blue line, and the present models using MUN05 PHOENIX+ new PoWR stellar library, in red line, for $Z = 0.004$ and CHA IMF. The bottom part of every sub-figure shows $\Delta L_{MI21-new} = \frac{L_{MI21}-L_{new}}{L_{MI21}}$.

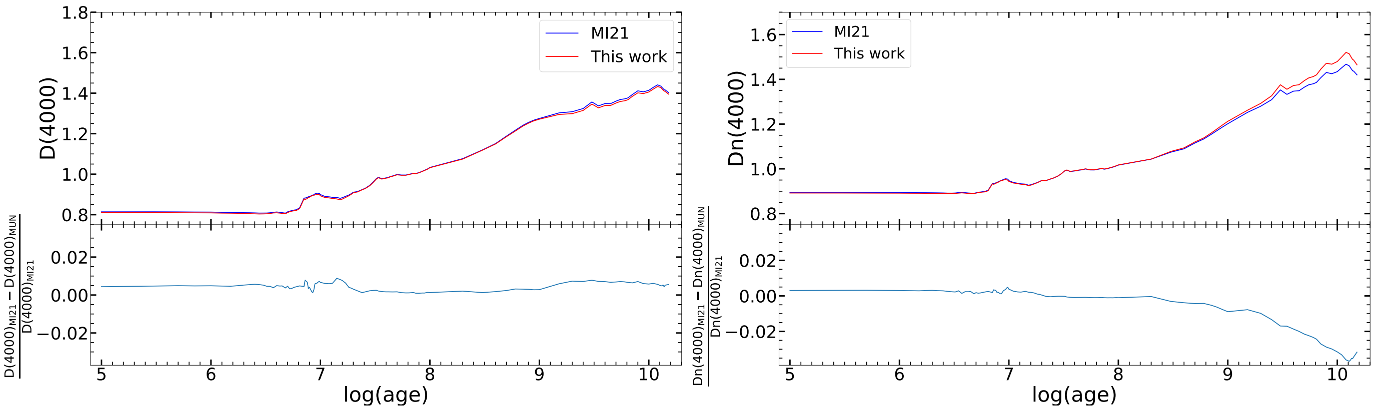

Fig. A.2. D4000 and Dn4000 break time evolution comparison for between MI21 in blue line and this work red line for $Z = 0.004$.

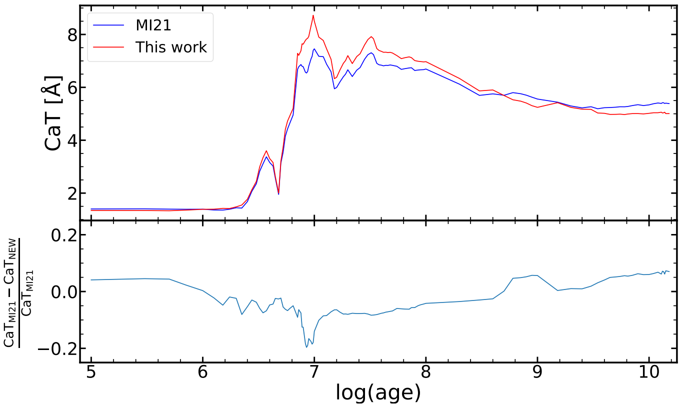

Fig. A.3. Calcium triplet break time evolution comparison for between MI21 in blue line and this work red line for Z = 0.004.

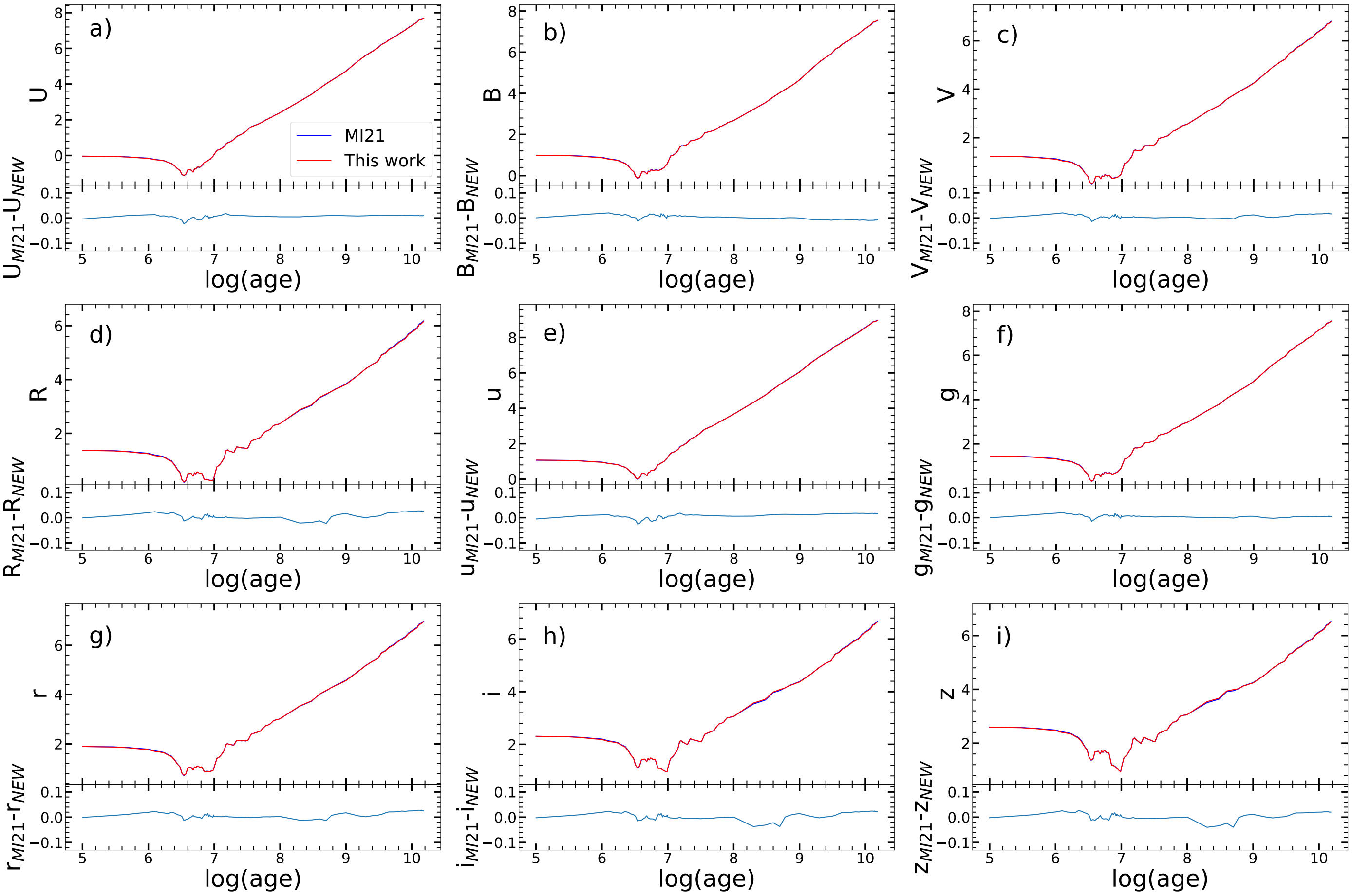

Fig. A.4. Evolution of magnitudes a) U, b) B, c) V, d) R, e) u, f) g, g) r, h) i, and i) z with age: comparison of results between MI21, blue, and this work, red, with residuals in the bottom panel for CHA IMF and Z = 0.004.